

Article

Paleoflood Reconstruction in the Lower Yellow River Floodplain (China) Based on Sediment Grain Size and Chemical Composition

Jinsong Yang ^{1,2,*} , Zhe Liu ², Jinhui Yin ^{1,*}, Liang Tang ³ , Hua Zhao ², Lei Song ² and Peng Zhang ⁴

¹ State Key Laboratory of Earthquake Dynamics, Institute of Geology, China Earthquake Administration, Beijing 100029, China

² Key Laboratory of Quaternary Chronology and Hydro-Environmental Evolution, Institute of Hydrogeology and Environmental Geology, China Geological Survey, Shijiazhuang 050061, China

³ College of Earth Sciences, Chengdu University of Technology, Chengdu 610059, China

⁴ Hebei Institute of Geological Survey, Shijiazhuang 050011, China

* Correspondence: yjs607@163.com (J.Y.); yjhdzs@ies.ac.cn (J.Y.)

Abstract: Alluvial sedimentary records in the North China Plain are essential in expanding flood history and understanding hazard patterns in the Yellow River basin where inundation risk exists and would probably increase under future global change. A detailed study of the Longwangmiao profile in the lower Yellow River floodplain reveals ancient flooding records over the late Holocene. Slackwater deposits are distinguished by typical sedimentary features and share similarities with those in the upper and middle Yellow River. This indicates that the traditional method can still be applied for paleoflood research beyond the gorge. However, unlike confined bedrock gorges, multiphase flood deposits of slackwater and overbank deposits represent different stages of flood events. These sedimentary assemblages recorded six flooding periods, further confirmed by the analysis of grain size and geochemistry. The profile was broadly subdivided into two flood-poor phases (3.7–6.7 ka, 0.8–1.7 ka) and three flood-rich phases (before 6.7 ka, 1.7–3.7 ka, after 0.8 ka) based on the dating results. Compared with the existing related research in the nearby area, the synchronous deposition cycles of floods and inter-floods are mainly controlled by the hydrodynamic conditions of the old Yellow River course. This study provides an analogue of paleoflood research in the lower Yellow River and similar alluvial plains. It explores the potential of interlinking paleoflood records in the whole Yellow River basin.

Keywords: paleoflood; Yellow River; North China Plain; late Holocene; grain size; major elements



Citation: Yang, J.; Liu, Z.; Yin, J.; Tang, L.; Zhao, H.; Song, L.; Zhang, P. Paleoflood Reconstruction in the Lower Yellow River Floodplain (China) Based on Sediment Grain Size and Chemical Composition. *Water* **2023**, *15*, 4268. <https://doi.org/10.3390/w15244268>

Academic Editors: Yaling Chen, Yuanxu Ma and Hongshan Gao

Received: 8 November 2023

Revised: 1 December 2023

Accepted: 4 December 2023

Published: 13 December 2023



Copyright: © 2023 by the authors. Licensee MDPI, Basel, Switzerland. This article is an open access article distributed under the terms and conditions of the Creative Commons Attribution (CC BY) license (<https://creativecommons.org/licenses/by/4.0/>).

1. Introduction

Floods are frequent natural disasters which often cause hundreds of thousands of lives and property to be lost annually. Recent studies argue that the frequency and intensity of floods are expected to continue to increase with climate change and global warming, especially in densely populated floodplains in Asia [1,2]. China is one of the most flood-prone countries in the world and has suffered from flood disasters for millennia. The Disaster Center reveals that ten out of the top 100 most deadly disasters of the 20th century were floods in China [3]. For instance, the recent “2021 Henan Flood” caused 398 deaths and 120.06 billion RMB Yuan (approx. USD 18.91 billion) in direct economic losses, according to the government disaster report [4]. Understanding the triggering mechanisms and risk changes has led researchers to extend flood records beyond the instrumental and historical period as paleoflood research [5–7].

Traditionally, most paleoflood studies heavily rely on slackwater deposits (SWDs) with sands and silts that accumulate in a relatively low-energy advection environment when the flood velocity is close to zero [8–11]. The global distribution of paleoflood research

illustrates the wealth of SWD sites in bedrock-confined settings [12,13]. Unfortunately, stable flood channel dimensions do not exist in most places, which severely limits the application of the SWD method and comprehensive analysis in the whole river basin. Lam et al. [14] stated that SWDs could be used beyond the traditional bedrock gorge through the research in subtropical Australia. Leigh [15] argued that overbank vertical accretion sediments (including SWDs) on the downstream floodplain are ubiquitous and continuous for paleoflood records. In contrast, SWDs in upper rivers are often fragmented and discontinuous. Thus, it is reasonable to infer that SWDs could be extended to much wider settings [16,17].

Alluvial plains exist in most river systems and hold enormous potential for paleoflood hydrology. The identification of paleoflood deposits and reconstruction of flood events have received increasing worldwide attention in the last decade [18,19]. Coarse grain size and typical elements are often used to detect flood archives in plains, such as the 95th percentile in the lower Rhine River [20], end-member modelling in the lower Meuse catchment, Netherland [21], and Zr/Fe in the lower Mississippi River, USA [22]. However, no single feature can typify the flood deposit in floodplain strata, and each index has multiple interpretations and uncertainty [23]. In addition, post-flood research indicated that the flood stratigraphy comprises multiphase sediments, normally including suspended coarse bedloads and fine-grained sediments related to different flood stages (e.g., [24–26]). Given the above, there is still a need for a better understanding of the characteristics of multiphase paleoflood deposits in low-lying regions.

The lower Yellow River (LYR) has witnessed extensive flooding hazards and has, therefore, deposited widespread flood sediments [27,28]. However, few studies have investigated paleofloods on the wide Yellow River floodplain, while extensive paleoflood research has been reported on the upstream and midstream over the past two decades [19,29]. Researchers recently found sedimentary flood records in archaeological sites and explored human–earth system interactions during historical periods [30–34]. These studies shed light on paleoflood sedimentary archives on the floodplain from the perspective of geoarchaeology. However, a detailed analysis of flood deposits and multi-proxy features has not been carried out.

Since 2016, exposed profiles have been investigated in abandoned channel areas of the LYR, where the Longwangmiao (LWM) profile is studied in detail due to its clear sedimentary characteristics [19]. This study conducts a comprehensive analysis of flood chronology, grain size, and geochemistry to reconstruct paleofloods with three main objectives: (1) to present the lithology, grain size, and main elements in different facies; (2) to demonstrate multiphase paleoflood deposits with SWDs and overbank deposits in the LYR; and (3) to reconstruct paleofloods and compare the result with regional research and historical records.

2. Regional Setting

The North China Plain (32° N–40° N, 112° E–122° E) has accumulated from alluvial lateral and vertical accretion deposits since the late Pleistocene [35,36]. It is one of China's most important social, economic, and agricultural regions, but it has been exposed to flood disasters for an extended period [37]. As recorded in historical documents, catastrophic levee failures occurred 1593 times, and the primary channel shifted 26 times in 4000 years [27,28]. Owing to its high susceptibility to perturbations, the LYR has left large amounts of paleochannels on the North China Plain [35,36] (Figure 1a). These topographic depressions in alluvial plains are suitable sites to preserve paleoflood deposits [15,18,38].

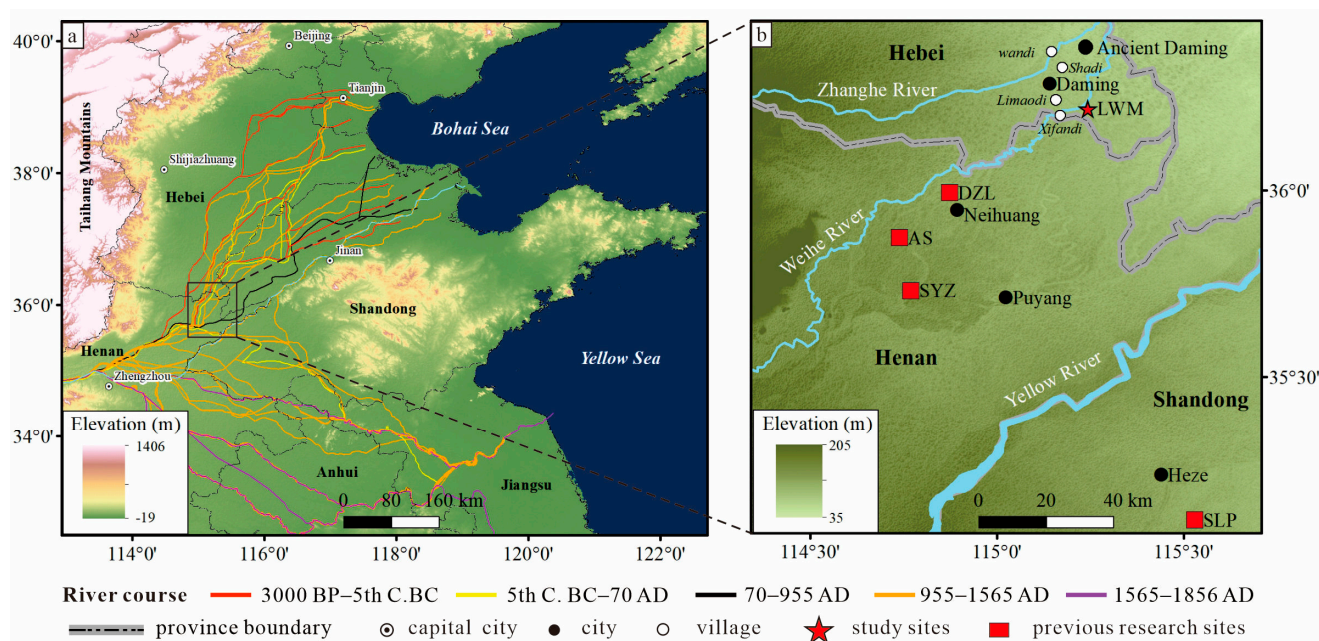


Figure 1. The sketch map of the study region. (a) The digital elevation model illustrates the North China Plain and historic abandoned channels of the Yellow River. The river course data are from [28]. (b) Topographic map showing the study area of the Neihuang-Daming counties. Previous research sites include the Dazhanglongcun (DZL) [31], Anshang (AS) [30], Sanyangzhuang (SYZ) [39], and Shilipu (SLP) sites [33].

The research area (Neihuang-Daming counties) is located southwest of the North China Plain. It belongs to the junction of Hebei, Shandong, and Henan provinces (Figure 1b). In Neihuang County, several alluvial geoarchaeological works have been carried out and uncovered a series of ancient flood records, including the Dazhanglongcun (DZL) [31], Anshang (AS) [30], Sanyangzhuang (SYZ) [39], and Shilipu (SLP) [33] sites. Few studies have been conducted in Daming County, although this county is rich in archaeological remains and has a long history with flood records. The ancient Daming county is located 8 km north of the county, which served as the northern capital in the Northern Song Dynasty (960–1127 AD, ca. 0.9–1.0 ka). Several floods were documented in this area, and the most severe inundation occurred in the third year of the Ming Dynasty (1401 AD, ca. 0.6 ka) when the ancient Daming county was submerged [40]. It has been further confirmed by archaeological work that the buildings were buried approx. 1–5 m below the surface by flood deposits [41,42].

The LWM profile (36°12′24″ N, 115°13′31″ E) is located about 10 km south of Daming County (Figure 1b). The LWM site is the floodplain depositional site next to the abandoned Yellow River, even though the landform evidence is no longer visible due to apparent modifications in agriculture and urbanization. Several villages, such as Dongmudi, Xifandi, and Limaodi (“di” means embank of rivers in Chinese), were located on ancient Yellow River embankments [40]. The evidence of paleochannel reconstruction from both the historical documentary [27,28] and the digital elevation model [43] also confirms the geomorphic setting of the sample site (Figure 1b). In this depositional environment, overbank flood sediments are prone to accumulate vertically and offer great potential for paleoflood research [15].

3. Material and Methods

Field samples of the LWM profile (depth of 9 m) were collected in 2018 with a detailed lithological description. The sedimentary characteristics were described, including colours, textures, structures, and stratigraphic contact relationships. Bulk samples were

obtained every 5 cm after detailed observation and stratigraphic subdivisions, and a total of 180 samples were collected to analyse grain size and geochemistry.

Optically stimulated luminescence (OSL) dating and radiocarbon dating were measured to confine the age of the deposits. Seven OSL samples, including six samples in overbank sands and one sample in paleosols, were collected by forcing a 5 cm diameter mental cylinder horizontally into sediments. Following the pretreatment process of OSL dating of flood sediments in the North China Plain [44], extracted quartz grains were measured using the single-aliquot regenerative-dose protocol [45,46] at the Key Laboratory of Quaternary Chronology and Hydro-Environmental Evolution, China Geological Survey. In addition, one ^{14}C sample in lacustrine deposits was given a full acid–base–acid pretreatment, including 1 M HCl (2 h, 60 °C), 0.1 M NaOH (overnight, 60 °C), and 1 M HCl (2 h, 60 °C) [47]. The sample was measured at Xi’an Accelerator Mass Spectrometry Centers, Shaanxi Province, China. The result is reported as radiocarbon ages in years before the present with an analytical precision better than 0.5%. Age calibration was carried out using the IntCal 20 calibration curve [48] and OxCal 4.4 (<https://c14.arch.ox.ac.uk>, accessed on 8 August 2023), which allows for direct comparison with OSL ages. The age–depth model of the stratigraphy sequence was then retrieved via Rbacon Rpackage using Bayesian statistics [49].

The particle size distributions of sediments were determined by adopting a Malvern Mastersizer 2000 after pretreatment with HCl (10%) and H_2O_2 (30%) to remove secondary carbonates and organic matter. The measurement ranged from 0.02 to 2000 μm in grain diameter, and the relative error was less than 1%. According to the classification method in the Yellow River paleoflood research, particle size was categorized into four groups: clay (<2 μm), fine silt (2–16 μm), coarse silt (16–63 μm), and sand (>63 μm) [50–52]. The compositions of the major elements (SiO_2 , Al_2O_3 , MgO , Fe_2O_3 , K_2O , Na_2O , and CaO) were measured using a PW4400 X-ray fluorescence spectrometer. In particular, 4.0 g of powdered samples (<200 mesh) and 2.0 g of boric acid were pressed into a pellet before measurement. The experiments were conducted at the Key Laboratory of Quaternary Chronology and Hydro-Environmental Evolution, China Geological Survey. Local polynomial regression (LOESS) of grain sizes and principal component analysis (PCA) of the elements were applied to statistically identify the sedimentation changes to support paleoflood reconstruction results [15,53,54].

The premise of a centred log–ratio (clr) transformation of elemental contents was applied to calibrate and reduce the matrix effects (e.g., variable water content and grain size distribution) [55,56]. Pearson’s correlation coefficients were calculated between the percentage of grain size fractions and elemental composition. PCA was conducted in R using the FactoMine R package [57] in order to examine co-variability among proxies and discriminate different sedimentary and geochemical processes [53,54]. Seven active variables of standardized major elements were applied to the analysis, and grain size fractions (including clay, fine silt, coarse silt, and sand) were plotted as supplementary variables.

4. Results

4.1. Stratigraphy

According to sedimentological criteria in the nearby sites, the lithology of the LWM profile can be summarized as sandy soil (SS), lacustrine deposit (LD), and overbank deposit (OD). The slackwater deposit (SWD) was separately analysed as a special type of overbank deposits, because it has been widely accepted as a paleoflood sedimentary evidence and has a ubiquitous distribution on the North China Plain [19,30,32,33]. The distinct lithological features of SWDs, mainly referred to the identification criteria within bedrock gorges [8,9,51,52], were summarized as follows: (1) consisting of silt and silty clay with laminated or massive structures; (2) abrupt vertical change of physical features, such as colour, grain size, and texture; (3) presence of buried soils or lacustrine sediments under SWDs; and (4) formation of a series of mud cracks on the layer surface, indicating surface exposure during non-flood periods. SWD layers were subdivided into six layers

through the sedimentological criteria. SWD2 (720–755 cm), SWD4 (430–495 cm), and SWD6 (110–190 cm) are much more obvious than SWD1 (890–900 cm) and SWD5 (320–330 cm), owing to their thicker layers and more stable features (Figure 2a).

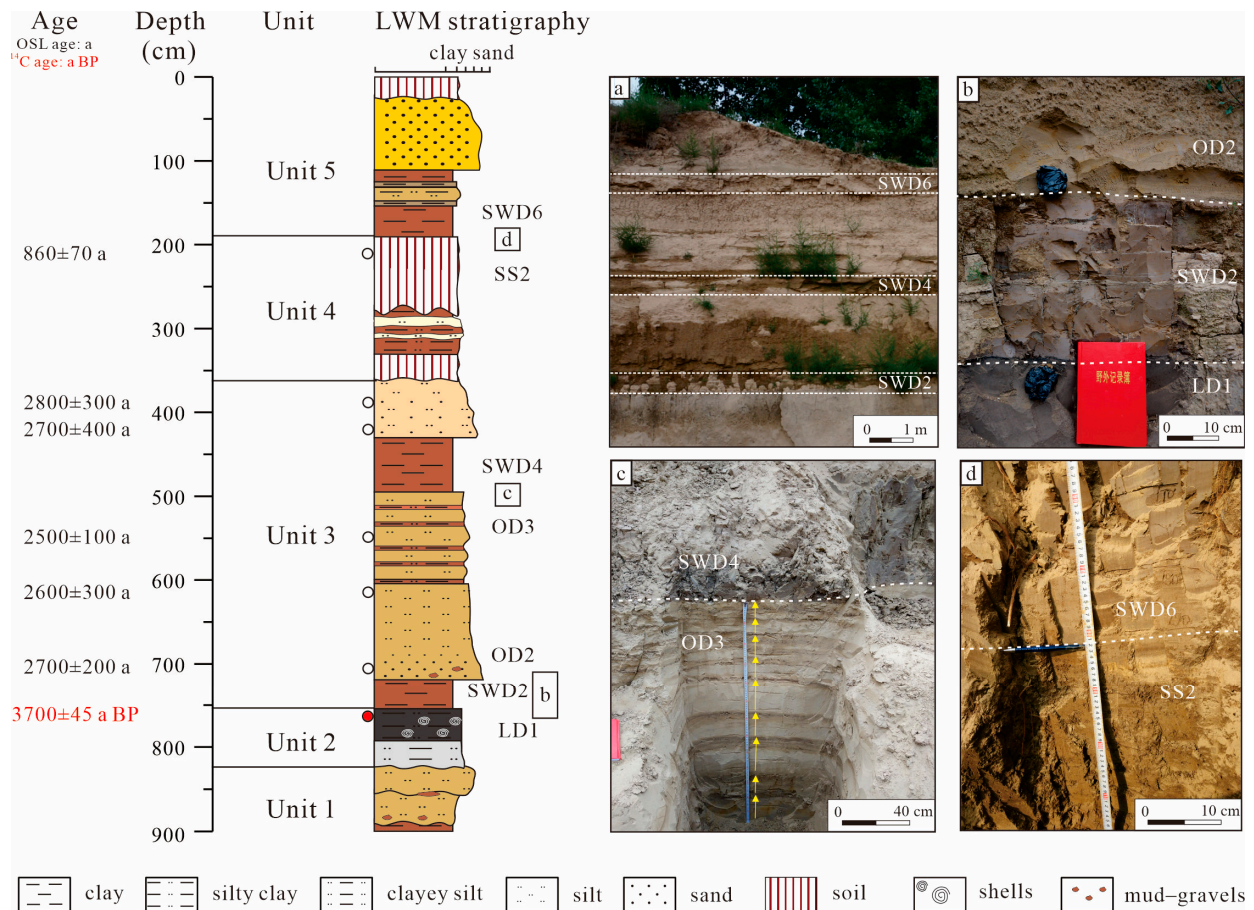


Figure 2. Sediment lithology and field photos of the LWM profile in the LYR. (a) Paleoflood SWDs with distinct lithological features in the profile. (b) LD1 with shells in Unit 2 overlain by SWD2 and OD2 in Unit 3. (c) Decimetre-scale fining-upward packages of OD3 (yellow arrows) overlain by structureless SWD4 in Unit 3. (d) SS2 overlain by structureless SWD6 in Unit 4. The dots represent the OSL and radiocarbon dating samples, and the radiocarbon dating result was different in red colour from the OSL results. The letter in rectangle shows the place of photos in (b–d), respectively.

The other deposits can be distinguished from SWDs by their colour, structure, and fossil remnants. In particular, ODs are mainly composed of yellow sand and red-brown silt, with cross-bedding and parallel bedding (Figure 2b,c). LDs are organic-rich dark grey silts (Figure 2b), and soils are brown and grey silty loams with abundant redoximorphic features (Figure 2d). The profile was finally divided into five units according to lithological features and assemblage (Table 1).

4.2. Chronology

Seven OSL dating results are listed in Table 2 and are consistent with the order of sedimentary stratigraphy. The OSL ages range from 7.2 ± 0.4 ka to 0.86 ± 0.07 ka and are mainly distributed around 2.5–2.8 ka in Unit 3, demonstrating that the fluvial sequence has been deposited rapidly during flood-rich periods. The result at the bottom of the profile is 7.2 ± 0.4 ka, indicating that the sedimentary rates varied in lacustrine deposits. One ¹⁴C age from the lacustrine bulk sample (Lab No. XA16700) at the depth of 7.56 m is 3700 ± 45 a BP, i.e., 4218–3901 cal a BP of 2σ calibrated age, that is consistent with the period of lake development in the North China Plain [35]. Furthermore, the topside OSL result

(0.86 ± 0.07 ka) in paleosol is consistent with regional archaeological work. The ancient Daming County was investigated to be buried 1–5 m below the surface by the flood deposits of the Ming Dynasty (ca. 0.6 ka) [42]. These flood deposits were tracked and correlated with Unit 5 in this study area (Figure 2).

Table 1. Stratigraphic descriptions, sedimentary facies, and lithological units in the LWM profile in the lower Yellow River.

Unit	Depth (cm)	Sedimentary Facies	Stratigraphic Description
5	0–20	Modern soil(SS3)	Grey-brown clay, crumb structure, friable and porous.
	20–110	Overbank deposit (OD6)	Grey-yellow fine sand, parallel laminations, very loose.
	110–190	Slackwater deposit (SWD6)	Red-brown clay, homogenous texture.
4	190–280	Paleosol (SS2)	Dark brown speckled clay, friable and porous.
	280–320	Overbank deposit (OD5)	Light yellow fine sand and red-brown clay couplet, parallel bedding.
	320–330	Slackwater deposit (SWD5)	Red-brown clay, homogenous texture.
	330–358	Paleosol (SS1)	Dark brown clay, friable and porous, crumb structure.
3	358–430	Overbank deposit (OD4)	Yellow-brown clayey silt, crumb structure, very loose.
	430–495	slackwater deposit (SWD4)	Red-brown clay, homogenous texture.
	495–600	Overbank deposit (OD3)	Grey-yellow silt with brown-red silty clay, dual structure, and parallel laminations.
	600–720	Overbank deposit (OD2)	Yellowish speckled fine sand, very loose, parallel laminations and ripples.
	720–755	Slackwater deposit (SWD2)	Red-brown clay, homogenous texture, some conchoidal fractures.
2	755–825	Lacustrine deposit (LD1)	Grey silty clay, few shells, massive structure.
1	825–890	Overbank deposit (OD1)	Grey-yellow silt, some mud-gravels at the bottom.
	890–900	slackwater deposit (SWD1)	Red-brown clay, homogenous texture, some conchoidal fractures.

Table 2. OSL ages of the LWM profile in the LYR.

Sample	Depth (m)	U (ppm)	Th (ppm)	K (%)	Water Content (%)	Equivalent Dose (Gy)	Dose Rate (Gy/ka)	Age (ka)
LWM-2	2	4.56 ± 0.23	24.01 ± 0.95	2.42 ± 0.06	15 ± 10	4.83 ± 0.06	5.62 ± 0.37	0.86 ± 0.07
LWM-3.8	3.8	2.47 ± 0.06	12.18 ± 0.17	1.67 ± 0.02	10 ± 5	8.13 ± 0.66	2.94 ± 0.11	2.8 ± 0.3
LWM-4.2	4.2	1.98 ± 0.1	9.67 ± 0.43	1.69 ± 0.03	10 ± 5	7.24 ± 0.93	2.69 ± 0.11	2.7 ± 0.4
LWM-5.5	5.5	1.61 ± 0.04	7.43 ± 0.13	1.66 ± 0.01	10 ± 5	7.05 ± 0.19	2.43 ± 0.1	2.5 ± 0.1
LWM-6.15	6.15	2.02 ± 0.05	8.82 ± 0.12	1.74 ± 0.05	15 ± 5	6.5 ± 0.74	2.54 ± 0.1	2.6 ± 0.3
LWM-7.1	7.1	2.17 ± 0.04	10.48 ± 0.18	1.61 ± 0.03	15 ± 5	8.33 ± 0.45	3.07 ± 0.18	2.7 ± 0.2
LWM-8.5	8.5	1.87 ± 0.06	9.26 ± 0.17	1.58 ± 0.06	10 ± 5	17.78 ± 0.57	2.48 ± 0.11	7.2 ± 0.1

4.3. Proxy Indicators

Grain size and major elemental contents can generally be used to divide the LWM profile into five units, consistent with the lithological units (Figure 3). The ages at the boundaries are generated from the age–depth model.

In Unit 1 (825–900 cm, before 6.7 ka), sediments are dominated by coarse silts (average 54.2%) and become coarser toward the top with an inverse grade. K_2O (average -0.91 clr) and Fe_2O_3 (average -0.27 clr) have the lowest value. SiO_2 (average 2.47 clr) and Na_2O (average -1.35 clr) have a relatively high value in upper samples. In comparison, Al_2O_3 (average 0.74 clr), CaO (average 0.31 clr), and MgO (average -0.98 clr) have a relatively high value at the bottom.

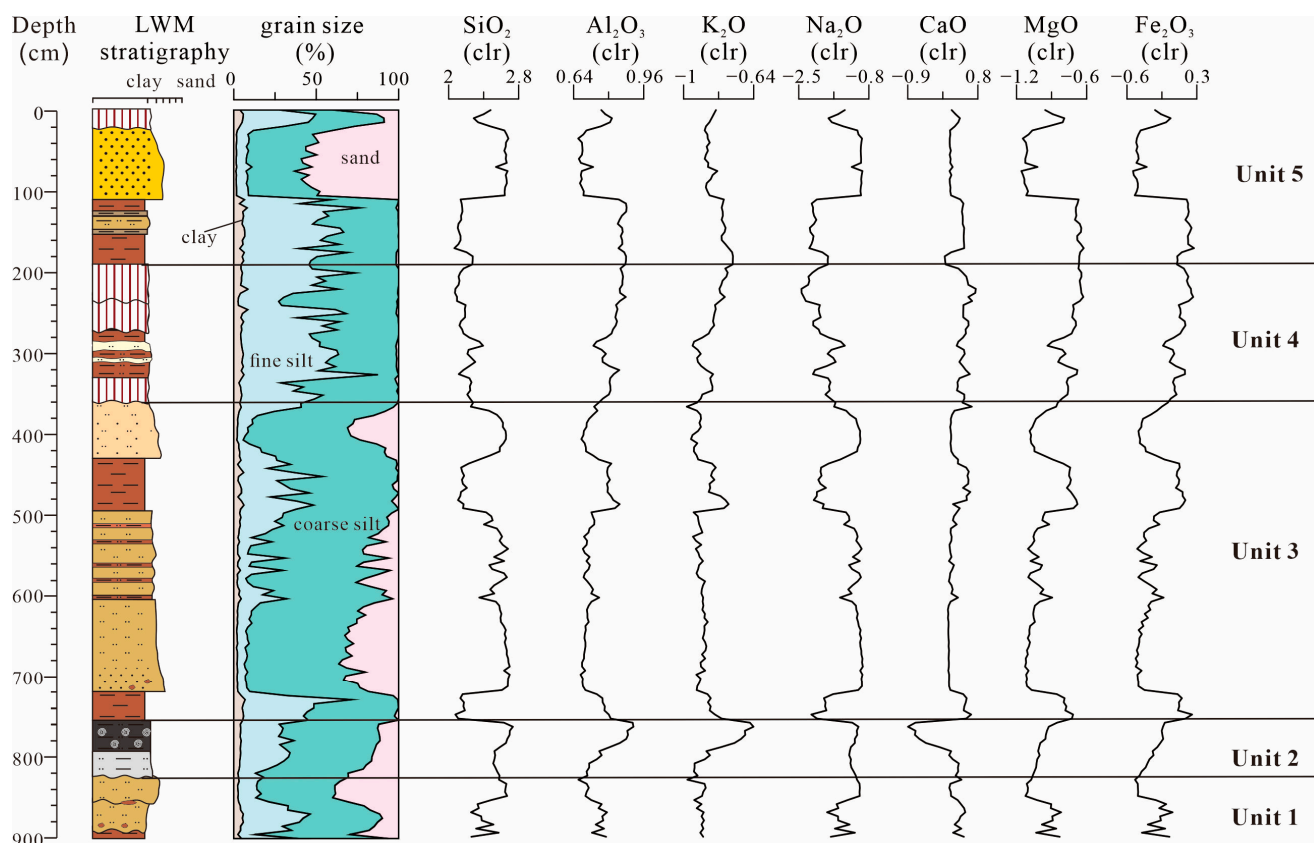


Figure 3. Stratigraphy, grain size composition, median grain size, and major elements variations in the LWM profile in the LYR. The legend is identical to that of Figure 2.

Unit 2 (755–825 cm, 3.7–6.7 ka) is characterised by a slow trend in proxy indicators and an abrupt change between LDs and ODs. Sediments are dominated by coarse silts (average 55.5%) and fine silts (average 23.7%). SiO_2 , K_2O , and Na_2O increase to a high average of 2.60 clr, -0.81 clr and -1.18 clr, respectively, while CaO (average -0.18 clr) and MgO (average -0.99 clr) have the lowest values.

Unit 3 (360–755 cm, 1.7–3.7 ka) is characterised by frequent changes in depth. The peak–valley variations in different proxy indicators are almost synchronous. Coarse silt (average 64.2%) increases to the maximum of the profile, while clay (average 3.11%) and fine silt (average 17.7%) have the lowest values. SiO_2 (average 2.48 clr), Na_2O (average -1.32), Al_2O_3 (average -0.72 clr), K_2O (average -0.90), CaO (average 0.24 clr), MgO (average -0.97 clr), and Fe_2O_3 (average -0.25 clr) remain with a similar average value but with much more obvious variations compared to Unit 2.

In Unit 4 (190–360 cm, 0.8–1.7 ka), sediments are much finer than in Unit 3. As fine silt (average 46.9%) and clay (average 4.74%) increase significantly, Al_2O_3 (average 0.82 clr), CaO (average 0.46 clr), MgO (average -0.73 clr), and Fe_2O_3 (average 0.08 clr) also have the highest value. Sand (average 0.7%), SiO_2 (average 2.19 clr), and Na_2O (average 1.96 clr) decrease to the lowest value of the profile. All the indicators fluctuate in a relatively tight range.

Unit 5 (0–190 cm, after 0.8 ka) has the highest value of sand (average 26.6%) and the lowest value of coarse sand (average 40.6%). SiO_2 and Na_2O increase to averages of 2.41 and -1.54 clr, respectively. Al_2O_3 (average 0.77 clr), K_2O (average -0.83 clr), MgO (average 0.77 clr), and Fe_2O_3 (average -0.89 clr) decrease slightly.

4.4. PCA

Significant correlations between the grain size and major elements are shown in Table 3. The percentage of sand is positively correlated with SiO_2 ($r = 0.79$) and Na_2O ($r = 0.77$). In

contrast, percentages of clay and fine silt have a strong positive correlation with Al_2O_3 , MgO , and Fe_2O_3 ($r > 0.75$), and a weak positive correlation with K_2O and CaO ($r < 0.5$). This result was supported by the biplot of the first two principal components (PC1 and PC2) (Figure 4). PC1 represents 76.80% of the total variance, having negative loadings for SiO_2 and Na_2O . The coarse silt and sand, as supplementary variables, are also plotted on the negative side of PC1. On the other hand, Al_2O_3 , K_2O , CaO , MgO , Fe_2O_3 , clay, and fine silt have positive loadings on PC1. The high percentage of SiO_2 and Na_2O is related to the dominance of quartz and plagioclase in the Yellow River, which originate primarily from the Loess Plateau [58,59]. Therefore, the first eigenvector (negative values) reflects the input evolution of coarse clastic deposits under strong hydrodynamic conditions, which was interpreted as a peak flood indicator to reconstruct paleofloods.

Table 3. Pearson’s correlation coefficients (r) between the major elemental contents and percentages of grain size fractions in the LWM profile.

Parameter	SiO_2	Al_2O_3	K_2O	Na_2O	CaO	MgO	Fe_2O_3	Clay	Fine Silt	Coarse Silt	Sand
SiO_2		-0.76 **	-0.37 **	0.98 **	-0.76 **	-0.96 **	-0.96 **	-0.76 **	-0.84 **	0.25 **	0.79 **
Al_2O_3			0.79 **	-0.83 **	0.21 **	0.90 **	0.90 **	0.75 **	0.79 **	-0.25 **	-0.73 **
K_2O				-0.47 **	-0.21 **	0.56 **	0.56 **	0.40 **	0.42 **	-0.26 **	-0.29 **
Na_2O					-0.71 **	-0.98 **	-0.97 **	-0.76 **	-0.84 **	0.28 **	0.77 **
CaO						0.58 **	0.56 **	0.42 **	0.51 **	-0.20 **	-0.43 **
MgO							0.99 **	0.79 **	0.86 **	-0.24 **	-0.82 **
Fe_2O_3								0.80 **	0.86 **	-0.23 **	-0.83 **
clay									0.92 **	-0.43 **	-0.75 **
fine silt										-0.53 **	-0.75 **
coarse silt											
silt											
sand											-0.16 *

Notes: **. Significant at $p < 0.01$. *. Significant at $p < 0.05$.

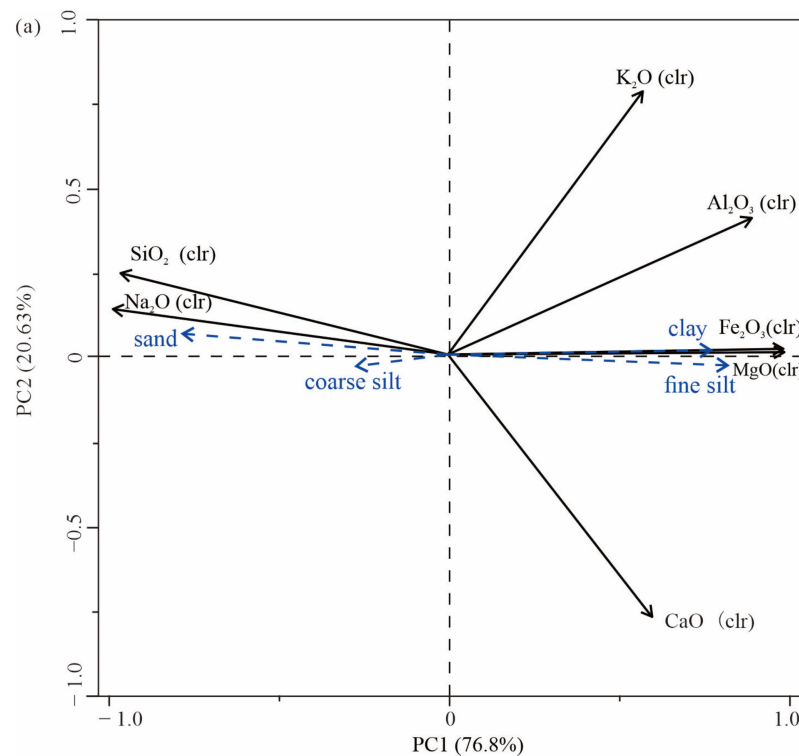


Figure 4. Cont.

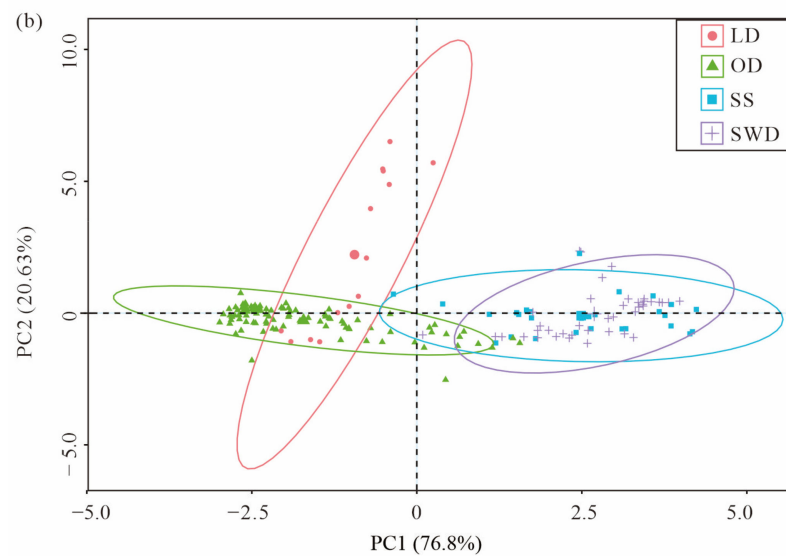


Figure 4. PCA biplot of the physicochemical parameters in the LWM profile in the LYR: (a) loading plot of standardized elemental data as active variables (solid black line), and grain size fractions as supplementary variables (dashed blue line). (b) The PCA score plot of samples in different facies.

5. Discussion

5.1. SWD as a Flood Indicator in the Yellow River Floodplain

SWDs in the LWM profile have distinct sedimentological and geochemical features with other sedimentary facies. SWDs are generally structureless, fine-grained sediments as a result of rapid deposition from suspension during major floods (Figure 2). It is noteworthy that both SS and SWD share relative similarities in particle sizes and major elements (Figure 4) because the pedogenesis on floodplains is mainly based on the previous alluvial deposit and accelerates finer sediments [60]. However, SS layers were distinguished by redoximorphic features and widely distributed proxies. Furthermore, the variation in the grain sizes and major elements with depth shows that SWDs have an abrupt change with adjacent deposits due to different hydrodynamic conditions (Figure 3). In general, the characteristics of SWDs are much more stable and significant than others.

The similarity of SWDs in different reaches of the Yellow River indicates that the SWD method for paleoflood identification can still be effective. Proxy indicators of SWDs are discussed by comparing the LWM profile with the upper and middle reaches of the Yellow River [50,61–63], providing a quantitative reference for further paleoflood research. The mean particle size of SWD2 (average: 19.12 μm), SWD4 (average: 23.62 μm), and SWD6 (average: 15.13 μm) in the LWM profile is much finer than the SWDs in the source area (51.87–55.05 μm , according to reference [63]), the upper reach (16.41–45.99 μm , according to reference [61]), and the middle reach (19.9–33.0 μm , according to reference [50]) (Figure 5). All SWDs in the Yellow River Basin have a narrow peak grain size distribution in common, indicating a similar suspension and deposition process in the flooding water. Additionally, SWDs have a gradual finer trend from the river source area to its lower reach, which reflects the sorting process of alluvial deposits with increasing transport distances [59].

Unlike traditional bedrock gorges, SWD is one type of multiphase flood deposits on alluvial plains. The deposition model with an ordered sequence of floodplain events indicates that SWDs were deposited at the beginning phase of flood [64]. This model has been confirmed by recent post-flood research [25,26]. In the LYR, geoarchaeological stratigraphy revealed that ancient flood deposits comprised red silty clay deposits, sandwiching a massive Yellow River silt flood package [30,32,33,39,65]. All SWDs in the LWM profile were covered by ODs of coarse silts and sands, especially SWD2/OD2, SWD4/OD4, and SWD6/OD6 with thick layers. According to previous studies on the sedimentation of a major flood in alluvial plains [24–26], the lower SWD layer was interpreted as the

deposition resulting from suspended sediments overtopped the levee, while the upper OD layer was interpreted as deposition resulting from the breached levee. In contrast, the SWD interpretation in canyons and gorges of the Yellow River is more direct because only high-stage SWDs were deposited during flooding periods, while other genetic deposits of non-fluvial environments (e.g., slope deposits or loess–paleosol) were accumulated during inter-flooding periods [50,51,66].

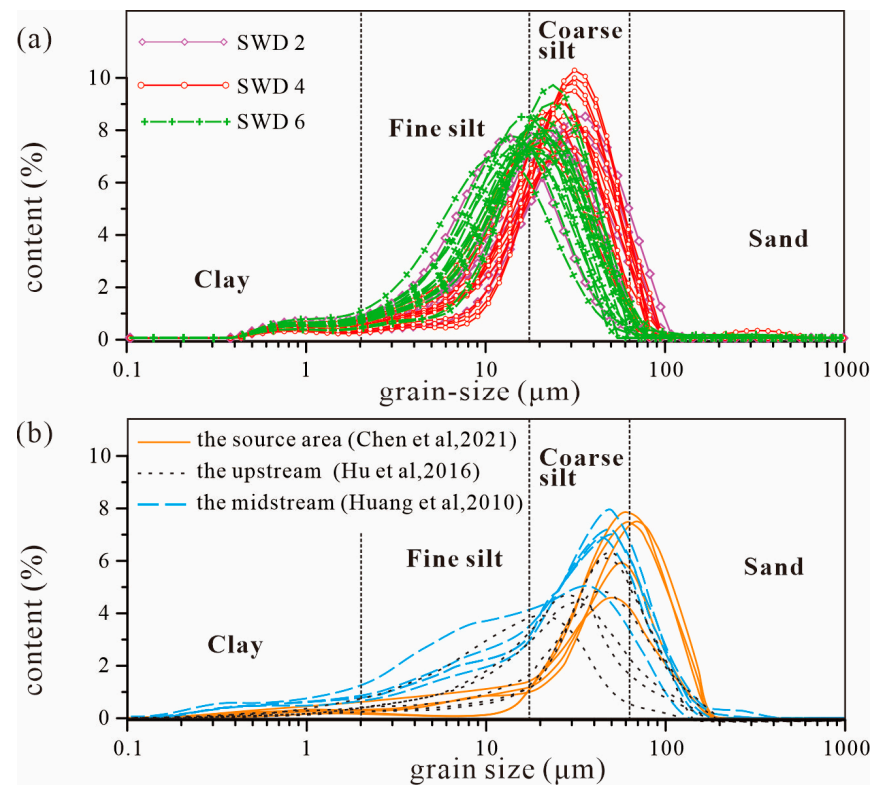


Figure 5. Frequency curve comparisons of the grain size distributions of SWDs between the LWM profile in the LYR (a) and typical research in the source area [63], the upper reach [61], and the middle reach [50] of the Yellow River (b).

High sedimentation rates and suitable depositional environments could be the key reasons why SWDs were preserved in the Yellow River floodplain. Two main factors controlling SWD deposition sites are appropriate sediment sources and preservation conditions [9,52]. The Yellow River, with the highest sediment load in the world [67], guarantees abundant sources of paleoflood deposits, and widely distributed low-lying regions in the LYR (e.g., back swamp and paleochannel) [35,36] provide container conditions for flood deposits. In short, our results suggest that the SWD method can be applied to the Yellow River floodplain and similar alluvial plains. A recent study on paleoflood reconstruction of the lower Ohio River, USA, also demonstrates the potential for SWD preservation in non-traditional alluvial settings [16].

5.2. Paleoflood Reconstruction and Regional Comparison

In order to verify the paleoflood stage indicator of SWDs, the LOESS of the sand [15,68] and PCA of elements [53,54] were applied as two widely accepted methods to reconstruct paleofloods in alluvial plains. Six flood periods (F1, F2, F3, F4, F5, and F6) in the LWM profile were reconstructed through the positive LOESS residuals and the regime shift in PC1 scores, which is consistent with paleoflood identification by SWDs (Figure 6). All except F3 have the corresponding depositional sequence with a stable SWD layer at the bottom and a thick OD layer at the top. F3 (495–600 cm) of silt–sand couplets differs from other floods by LOESS residuals and PC1 scores repeated change (Figure 6). Previous

studies have indicated that each fining-up sequence represents a short-term interval of the whole flood in the modern Yellow River delta [69]. Thus, F3 was interpreted as seasonal flooding deposits. On the other hand, F1 (825–900 cm), F2 (600–755 cm), F4 (358–495 cm), F5 (280–330 cm), and F6 (20–190 cm) have a significant change in reconstruction indicators.

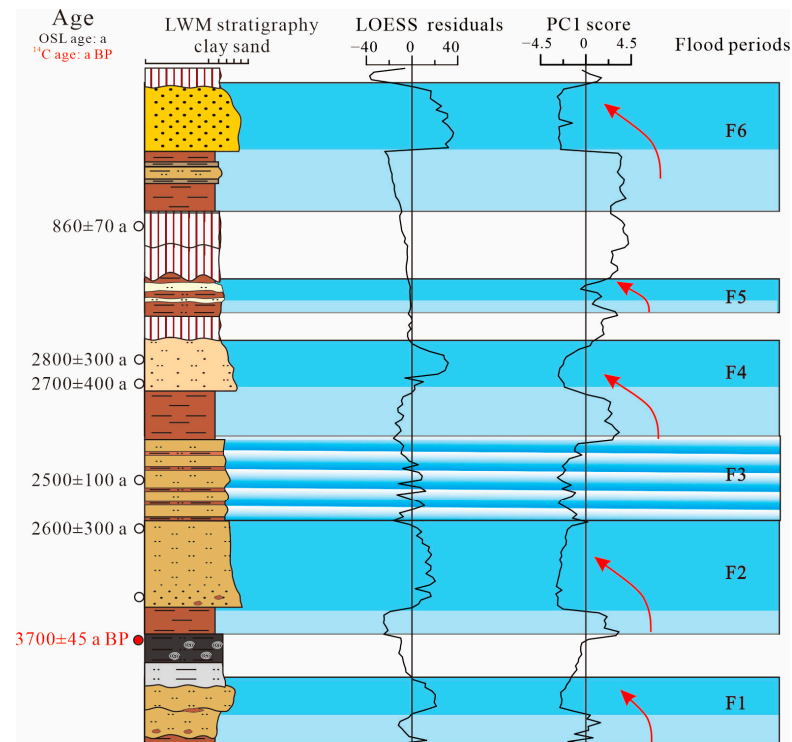


Figure 6. Paleoflood reconstruction in the LWM profile based on LOESS residuals and PC1 scores. The red arrow represents the subtle variation in flood deposits with blue color. F3 in different pattern as its result show rhythmic changes. The legend is identical to that of Figure 2.

The LWM stratigraphy was further subdivided into flood-rich and flood-poor phases based on the stratigraphy and chronology. In spite of F5, Unit 2 (3.7–6.7 ka) and Unit 4 (0.8–1.7 ka) were formed in a relatively stable environment during flood-poor phases. F5, showing a subtle variation in PC1 scores and LOESS residuals in Figure 6, suggested the flood magnitude is at a lesser level. On the contrary, Unit 1 (before 6.7 ka), Unit 3 (1.7–3.7 ka), and Unit 5 (after 0.8 ka) represent flood-rich phases, especially Unit 3 with F2, F3, and F4. This serious flooding phase around 4.0 ka was supported by existing research. The integration of the related dating results in a recent review paper shows that the relative concentration of paleoflood events occurred since ca. 4.0 ka in the Yellow River basin [29,70].

The paleoflood reconstruction in the LWM profile can be further supported by geoarchaeological evidence in the Yellow River floodplain. AS, DZL, SYZ, and SLP sites (Figure 1b) were chosen to compare in the study area because (1) they are archaeological sites with reliable chronology based on ceramic vessels, architectural tiles and dating results; and (2) they preserved similar sedimentary sequences in the adjacent area [30,31,39,71].

As shown in Figure 7, our results are difficult to use for confirming historical inundation events due to the dating inaccuracy and stratigraphic break. However, these synchronical ages of paleoflood deposits in all the sites imply that the regional flood events may have worsened around the Han Dynasty and Song Dynasty, while the river was inactive in the interval. As Figure 1 shows, the old Yellow River courses were mainly distributed in the study area around the 5th C. BC–70 AD (around the Han Dynasty) and 955–1565 AD (around the Song Dynasty). This statement agrees with the increased flood frequency in the last millennium by synthesizing sedimentary and documentary data of

the Yellow River basin [70]. In addition, the top F6 in Figure 7 was only recorded in the LWM profile. The reason is that the last flood was the extreme regional flood in the Daming area, as recorded in the documentary [40].

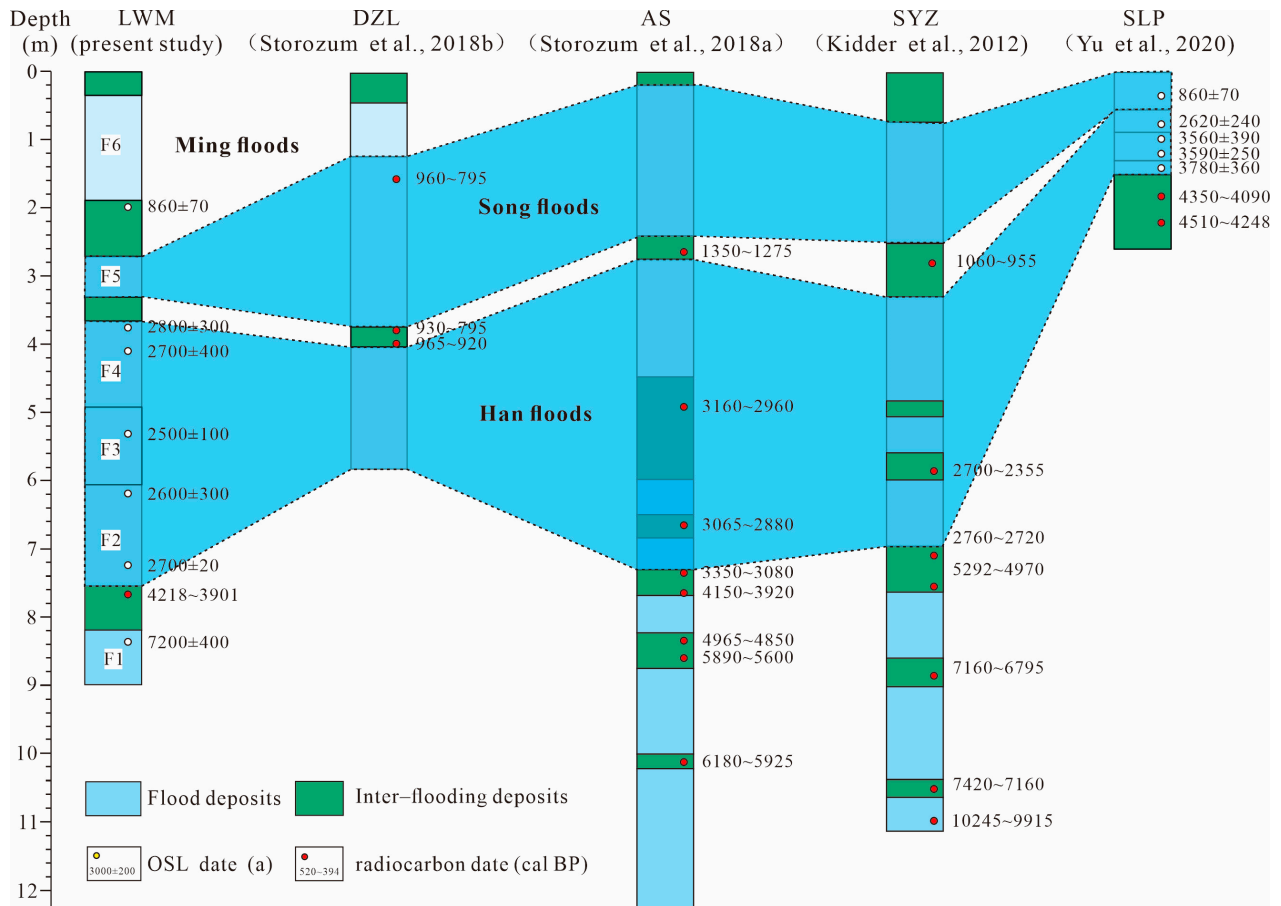


Figure 7. Comparison of extreme floods in the LWM profile with previous research profiles in the LYR. The Dazhanglongcun (DZL) site was modified from [31]; the Anshang (AS) site was modified from [30]; the Sanyangzhuang (SYZ) site was modified from [39]; and the Shilipu (SLP) site was modified from [33].

The correlation also suggests that the stratigraphy sequence and depositional rate in flood-prone floodplains are matched. The flooding and inter-flooding units are mainly controlled by the hydrodynamic conditions of the old Yellow River. For instance, the SYZ and LWM sites exhibited similar flood deposits among F2, F3, and F4 around the Han Dynasty. Seasonal flood deposits (F3) are composed of thin silt and silty clay, while major flood deposits (F2 and F4) mainly contain thick SWD and OD layers representing different flood stages (Figure 2c). In the SYZ site, the flood deposit consists of an initial fine-grained massive deposit that gradually transitioned to a silt loam/silty clay loam and then abruptly shifted to laminated silt and silty clay stratum [39]. These depositional assemblages and features are consistent with our lithological observation, suggesting sedimentary features of breach or diversion on the floodplain are similar and comparable [24–26]. Noteworthy, the SLP site has a different sediment rate from the others because it is a typical mound site which is significantly higher than the surrounding ground and accumulated by human activities [33,72].

The research highlights the potential to reconstruct long-term paleoflood series on the alluvial plain. Compared to widespread flooding records in the middle river, paleoflood research in the LYR is still limited and challenging [19]. However, interlinking disaster mechanisms in river systems need more detailed archives on floodplains to be better

revealed [13,73]. Further work is required to uncover the paleodischarge of flood deposits and explore the linkages between flood signatures and major factors.

6. Conclusions

The study focuses on the sedimentological and geochemical features of the LWM profile in the Yellow River floodplain in order to identify and reconstruct paleoflood events. SWDs in the LYR have distinct features with other sedimentary facies, but they are comparable with SWDs in the upper and middle Yellow River. This suggests that the SWD method can be applied in the LYR due to its high sedimentary rates and suitable depositional environments. Six flooding periods, including major and seasonal floods, were identified based on sedimentary characteristics, major elemental compositions, and particle size distribution. Our results display that Unit 2 (3.7–6.7 ka) and Unit 4 (0.8–1.7 ka) correspond to a relatively stable environment during flood-poor phases, while Unit 1 (before 6.7 ka), Unit 3 (1.7–3.7 ka), and Unit 5 (after 0.8 ka) correspond to flood-rich phases. These paleohydrology characteristics are broadly consistent with those in regional stratigraphy and historical documentaries, which confirms that sedimentological and geochemical analysis are effective methods for paleoflood research in the Yellow River. The low-lying floodplain is extremely vulnerable to inundations, leading to challenging work on paleoflood reconstruction. Nevertheless, the method linking to multi-proxy analysis provides an optimal geological point to understand flood features and explore paleoflood records on the floodplain, where there is an increasing flood risk with population growth, rapid urbanization, and economic growth development.

Author Contributions: Conceptualization, methodology and writing, J.Y. (Jinsong Yang), Z.L. and L.T.; formal analysis, J.Y. (Jinsong Yang), L.T. and H.Z.; investigation, J.Y. (Jinsong Yang), L.S. and P.Z.; supervision, J.Y. (Jinhui Yin); funding acquisition, J.Y. (Jinsong Yang) and J.Y. (Jinhui Yin). All authors have read and agreed to the published version of the manuscript.

Funding: This work was supported by the National Natural Science Foundation of China (no. 41807428), the Natural Science Foundation of Hebei Province (no. D2020504008), the IGCEA Project Funding (no. IGCEA1903), and the Basic Research Program of Chinese Academy of Geological Sciences (no. YK202308).

Data Availability Statement: The data supporting this study's findings are available from the corresponding author upon reasonable request.

Acknowledgments: The authors thank Qiuyao Dong for assistance with elemental analysis. We sincerely thank Mark Macklin, Gertruda Zieniute, and Harry Roberts from the University of Lincoln, United Kingdom, for their proofreading and revising the paper's language. We are grateful to the editor and anonymous reviewers for their constructive suggestions.

Conflicts of Interest: The authors declare that they have no known competing financial interest or personal relationships that could have appeared to influence the work reported in this paper.

Abbreviations

LYR	lower Yellow River
SWD	slackwater deposit
LD	lacustrine deposit
OD	overbank deposit
SS	sandy soil
OSL	optically stimulated luminescence
LWM	Longwangmiao
DZL	Dazhanglongcun
AS	Anshang
SYZ	Sanyangzhuang
SLP	Shilipu
LOESS	local polynomial regression
PCA	principal component analysis
ka	thousand years before the present

References

1. Merz, B.; Blöschl, G.; Vorogushyn, S.; Dottori, F.; Aerts, J.C.J.H.; Bates, P.; Bertola, M.; Kemter, M.; Kreibich, H.; Lall, U.; et al. Causes, impacts and patterns of disastrous river floods. *Nat. Rev. Earth Environ.* **2021**, *2*, 592–609. [[CrossRef](#)]
2. Tellman, B.; Sullivan, J.A.; Kuhn, C.; Kettner, A.J.; Doyle, C.S.; Brakenridge, G.R.; Erickson, T.A.; Slayback, D.A. Satellite imaging reveals increased proportion of population exposed to floods. *Nature* **2021**, *596*, 80–86. [[CrossRef](#)] [[PubMed](#)]
3. The Most Deadly 100 Natural Disasters of the 20th Century. Available online: https://www.disastercenter.com/disaster/TOP100_K.html (accessed on 8 November 2023).
4. Xu, J.; Li, R.; Zhang, Q.; Chen, Y.; Liang, X.; Gu, X. Extreme large-scale atmospheric circulation associated with the “21·7” Henan flood. *Sci. China Earth Sci.* **2022**, *65*, 1847–1860. [[CrossRef](#)]
5. Kochel, R.C.; Baker, V.R. Paleoflood hydrology. *Science* **1982**, *215*, 353–361. [[CrossRef](#)] [[PubMed](#)]
6. St. George, S.; Hefner, A.M.; Avila, J. Paleofloods stage a comeback. *Nat. Geosci.* **2020**, *13*, 766–768. [[CrossRef](#)]
7. Reinders, J.B. Extending flood records of rivers with sediment records. *Nat. Rev. Earth Env.* **2022**, *3*, 425. [[CrossRef](#)]
8. Baker, V.R. Paleoflood hydrology and extraordinary flood events. *J. Hydrol.* **1987**, *96*, 79–99. [[CrossRef](#)]
9. Benito, G.; Sánchez-Moya, Y.; Sopena, A. Sedimentology of high-stage flood deposits of the Tagus River, Central Spain. *Sediment. Geol.* **2003**, *157*, 107–132. [[CrossRef](#)]
10. Guo, Y.; Ge, Y.; Mao, P.; Liu, T. A comprehensive analysis of Holocene extraordinary flood events in the Langxian gorge of the Yarlung Tsangpo River valley. *Sci. Total Environ.* **2023**, *863*, 160942. [[CrossRef](#)]
11. Mao, P.; Guo, Y.; Liu, T. Holocene extreme palaeofloods recorded by slackwater deposits along the Jiacha Gorge of the Yarlung Tsangpo River valley, southern Tibetan Plateau. *Catena* **2023**, *231*, 107360. [[CrossRef](#)]
12. Wilhelm, B.; Ballesteros Canovas, J.A.; Corella Aznar, J.P.; Kämpf, L.; Swierczynski, T.; Stoffel, M.; Støren, E.; Toonen, W. Recent advances in paleoflood hydrology: From new archives to data compilation and analysis. *Water Secur.* **2018**, *3*, 1–8. [[CrossRef](#)]
13. Baker, V.R.; Benito, G.; Brown, A.G.; Carling, P.A.; Enzel, Y.; Greenbaum, N.; Herget, J.; Kale, V.S.; Latrubesse, E.M.; Macklin, M.G.; et al. Fluvial palaeohydrology in the 21st century and beyond. *Earth Surf. Process. Landf.* **2022**, *47*, 58–81. [[CrossRef](#)]
14. Lam, D.; Croke, J.; Thompson, C.; Sharma, A. Beyond the gorge: Palaeoflood reconstruction from slackwater deposits in a range of physiographic settings in subtropical Australia. *Geomorphology* **2017**, *292*, 164–177. [[CrossRef](#)]
15. Leigh, D.S. Vertical accretion sand proxies of gaged floods along the upper Little Tennessee River, Blue Ridge Mountains, USA. *Sediment. Geol.* **2018**, *364*, 342–350. [[CrossRef](#)]
16. Wiman, C.; Harden, T.; Shen, Z.; Curry, B.B.; Reinders, J.B.; Beighley, R.E.; Muñoz, S.E. Large floods on the lower Ohio River inferred from slackwater deposits. *Progress Phys. Geogr. Earth Environ.* **2023**. [[CrossRef](#)]
17. Jones, A.P.; Shimazu, H.; Oguchi, T.; Okuno, M.; Tokutake, M. Late Holocene slackwater deposits on the Nakagawa River, Tochigi Prefecture, Japan. *Geomorphology* **2001**, *39*, 39–51. [[CrossRef](#)]
18. Toonen, W.H.J.; Munoz, S.E.; Cohen, K.M.; Macklin, M.G. High-Resolution Sedimentary Paleoflood Records in Alluvial River Environments: A Review of Recent Methodological Advances and Application to Flood Hazard Assessment. In *Palaeohydrology (Traces, Tracks and Trails of Extreme Events)*; Herget, J., Fontana, A., Eds.; Springer: Cham, Switzerland, 2020; pp. 213–228.
19. Yang, J.; Wang, Y.; Yin, J.; Zhao, H.; Liu, Z.; Jiang, G.; Zhang, P.; Qi, J. Progress and Prospects in the Reconstruction of Flood Events in Chinese Alluvial Plains. *Earth Sci.* **2022**, *11*, 3944–3959. (In Chinese with English Abstract) [[CrossRef](#)]
20. Toonen, W.H.J.; Winkels, T.G.; Cohen, K.M.; Prins, M.A.; Middelkoop, H. Lower Rhine historical flood magnitudes of the last 450 years reproduced from grain-size measurements of flood deposits using End Member Modelling. *Catena* **2015**, *130*, 69–81. [[CrossRef](#)]
21. Peng, F.; Prins, M.A.; Kasse, C.; Cohen, K.M.; Van der Putten, N.; van der Lubbe, J.; Toonen, W.H.J.; van Balen, R.T. An improved method for paleoflood reconstruction and flooding phase identification, applied to the Meuse River in the Netherlands. *Glob. Planet. Chang.* **2019**, *177*, 213–224. [[CrossRef](#)]
22. Munoz, S.E.; Gruley, K.E.; Massie, A.; Fike, D.A.; Schroeder, S.; Williams, J.W. Cahokia’s emergence and decline coincided with shifts of flood frequency on the Mississippi River. *Proc. Natl. Acad. Sci. USA* **2015**, *112*, 6319–6324. [[CrossRef](#)] [[PubMed](#)]
23. Hagstrom, C.A.; Leckie, D.A.; Smith, M.G. Point bar sedimentation and erosion produced by an extreme flood in a sand and gravel-bed meandering river. *Sediment. Geol.* **2018**, *377*, 1–16. [[CrossRef](#)]
24. Li, C.; Zhang, Y. Flood sedimental characteristic and its mark on the middle reaches of Yangtze River. *Adv. Water Resour.* **2004**, *15*, 485–488.
25. Dan, M.; Sawai, Y.; Yamada, M.; Namegaya, Y.; Shinozaki, T.; Takeda, D.; Fujino, S.; Tanigawa, K.; Nakamura, A.; Pilarczyk, J.E. Erosion and sedimentation during the September 2015 flooding of the Kinu River, central Japan. *Sci. Rep.* **2016**, *6*, 34168. [[CrossRef](#)]
26. Knight, J.; Evans, M. The sediment stratigraphy of a flood event: An example from the Sabie River, South Africa. *Catena* **2017**, *151*, 87–97. [[CrossRef](#)]
27. Chen, Y.; Syvitski, J.P.M.; Gao, S.; Overeem, I.; Kettner, A.J. Socio-economic Impacts on Flooding: A 4000-Year History of the Yellow River, China. *Ambio* **2012**, *41*, 682–698. [[CrossRef](#)] [[PubMed](#)]
28. Chen, Y. Flood dynamics of the lower Yellow River over the last 3000 years: Characteristics and implications for geoarchaeology. *Quatern. Int.* **2019**, *521*, 147–157. [[CrossRef](#)]

29. Wang, H.; Jia, Y.; Zhang, Y.; Wang, N.; Luo, P.; Qiu, H.; Ayidina, S.; Xiao, Q.; Chen, D. Research progress of paleoflood events in the Yellow River Basin since the Last Deglaciation. *Progress Geogr.* **2021**, *40*, 1220–1234. (In Chinese with English Abstract) [[CrossRef](#)]
30. Storozum, M.; Liu, H.; Qin, Z.; Ming, K.; Fu, K.; Wang, H.; Kidder, T. Early evidence of irrigation technology in the North China Plain: Geoarchaeological investigations at the Anshang Site, Neihuang County, Henan Province, China. *Geoarchaeology* **2018**, *33*, 143–161. [[CrossRef](#)]
31. Storozum, M.; Qin, Z.; Ren, X.; Li, H.; Cui, Y.; Fu, K.; Liu, H. The collapse of the North Song dynasty and the AD 1048–1128 Yellow River floods: Geoarchaeological evidence from northern Henan Province, China. *Holocene* **2018**, *28*, 1759–1770. [[CrossRef](#)]
32. Storozum, M.; Lu, P.; Wang, S.; Chen, P.; Yang, R.; Ge, Q.; Cao, J.; Wan, J.; Wang, H.; Qin, Z.; et al. Geoarchaeological evidence of the AD 1642 Yellow River flood that destroyed Kaifeng, a former capital of dynastic China. *Sci. Rep.* **2020**, *10*, 3765. [[CrossRef](#)]
33. Yu, S.; Hou, Z.; Chen, X.; Wang, Y.; Song, Y.; Gao, M.; Pan, J.; Sun, M.; Fang, H.; Han, J.; et al. Extreme flooding of the lower Yellow River near the Northgrippian-Meghalayan boundary: Evidence from the Shilipu archaeological site in southwestern Shandong Province, China. *Geomorphology* **2020**, *350*, 106878. [[CrossRef](#)]
34. Qin, Z.; Storozum, M.J.; Liu, H.; Kidder, T.R. Holocene landscape evolution in northern Henan Province and its implications for archaeological surveys. *Geoarchaeology* **2022**, *38*, 320–334. [[CrossRef](#)]
35. Wu, C.; Xu, Q.; Ma, Y.; Zhang, X. Palaeochannels on the North China Plain: Palaeoriver geomorphology. *Geomorphology* **1996**, *18*, 37–45. [[CrossRef](#)]
36. Wu, C.; Xu, Q.; Zhang, X.; Ma, Y. Palaeochannels on the North China Plain: Types and distributions. *Geomorphology* **1996**, *18*, 5–14. [[CrossRef](#)]
37. Liu, C.; Yu, J.; Eloise, K. Groundwater exploitation and its impact on the environment in the North China Plain. *Water Int.* **2001**, *26*, 265–272.
38. Jones, A.F.; Lewin, J.; Macklin, M.G. Flood series data for the later Holocene: Available approaches, potential and limitations from UK alluvial sediments. *Holocene* **2010**, *20*, 1123–1135. [[CrossRef](#)]
39. Kidder, T.R.; Liu, H.; Li, M. Sanyangzhuang: Early farming and a Han settlement preserved beneath Yellow River flood deposits. *Antiquity* **2012**, *86*, 30–47. [[CrossRef](#)]
40. Daming County Local Gazetteers Compilation Committee. Natural disaster. In *Daming County Local Gazetteers*; Xinhua Publishing House: Beijing, China, 1994; pp. 99–112.
41. Liang, H.; Wei, Z. The history and its value of ancient Daming Palace. *China Anc. City* **2011**, 42–47. (In Chinese with English Abstract)
42. Bai, X.; Wu, Z.; Zhang, Y.; Lu, G.; Liu, C.; Ren, X.; Xu, Y. Survey of the ancient city of Daming Palace, Hebei Province. *Cult. Relics Age* **2015**, *5*, 27–34. (In Chinese)
43. Zhang, S.; Ma, Y.; Chen, F.; Liu, J.; Chen, F.; Lu, S.; Jiang, L.; Li, D. A new method for supporting interpretation of paleochannels in a large scale—Detrended Digital Elevation Model Interpretation. *Geomorphology* **2020**, *369*, 107374. [[CrossRef](#)]
44. Zhao, H.; Liu, Z.; Song, L.; Wang, C.; Li, S. OSL dating of flood sediments in the North China Plain. *Quat. Geochronol.* **2019**, *49*, 101–107. [[CrossRef](#)]
45. Murray, A.S.; Wintle, A.G. Luminescence dating of quartz using an improved single-aliquot regenerative-dose protocol. *Radiat. Meas.* **2000**, *32*, 57–73. [[CrossRef](#)]
46. Wintle, A.G.; Murray, A.S. A review of quartz optically stimulated luminescence characteristics and their relevance in single-aliquot regeneration dating protocols. *Radiat. Meas.* **2006**, *41*, 369–391. [[CrossRef](#)]
47. Cheng, P.; Fu, Y. Stepped-combustion ¹⁴C dating in loess-paleosol sediment. *Radiocarbon* **2020**, *62*, 1209–1220. [[CrossRef](#)]
48. Reimer, P.J.; Austin, W.E.N.; Bard, E.; Bayliss, A.; Blackwell, P.G.; Bronk Ramsey, C.; Butzin, M.; Cheng, H.; Edwards, R.L.; Friedrich, M.; et al. The IntCal20 Northern Hemisphere Radiocarbon Age Calibration Curve (0–55 cal kBP). *Radiocarbon* **2020**, *62*, 725–757. [[CrossRef](#)]
49. Blaauw, M.; Christen, J.A. Flexible paleoclimate age-depth models using an autoregressive gamma process. *Bayesian Anal.* **2011**, *6*, 457–474. [[CrossRef](#)]
50. Huang, C.C.; Pang, J.; Zha, X.; Zhou, Y.; Su, H.; Li, Y. Extraordinary Floods of 4100–4000 a BP recorded at the Late Neolithic Ruins in the Jinghe River Gorges, Middle Reach of the Yellow River, China. *Palaeogeogr. Palaeoclimatol. Palaeoecol.* **2010**, *289*, 1–9. [[CrossRef](#)]
51. Huang, C.C.; Pang, J.; Zha, X.; Su, H.; Jia, Y. Extraordinary floods related to the climatic event at 4200 a BP on the Qishuihe River, middle reaches of the Yellow River, China. *Quat. Sci. Rev.* **2011**, *30*, 460–468. [[CrossRef](#)]
52. Zhang, Y.; Huang, C.C.; Pang, J.; Zha, X.; Zhou, Y.; Yin, S.; Wang, J. Comparative study of the modern flood slackwater deposits in the upper reaches of Hanjiang and Weihe River Valleys, China. *Quatern. Int.* **2012**, *282*, 184–191. [[CrossRef](#)]
53. Moreno, A.; Valero-Garcés, B.L.; González-Sampériz, P.; Rico, M. Flood response to rainfall variability during the last 2000 years inferred from the Taravilla Lake record (Central Iberian Range, Spain). *J. Paleolimnol.* **2008**, *40*, 943–961. [[CrossRef](#)]
54. Affouri, A.; Dezileau, L.; Kallel, N. Extreme flood event reconstruction spanning the last century in the El Bibane Lagoon (southeastern Tunisia): A multi-proxy approach. *Clim. Past* **2017**, *13*, 711–727. [[CrossRef](#)]
55. Weltje, G.J.; Tjallingii, R. Calibration of XRF core scanners for quantitative geochemical logging of sediment cores: Theory and application. *Earth Planet. Sci. Lett.* **2008**, *274*, 423–438. [[CrossRef](#)]

56. Weltje, G.J.; Bloemsa, M.R.; Tjallingii, R.; Heslop, D.; Röhl, U.; Croudace, I.W. *Prediction of Geochemical Composition from XRF Core Scanner Data: A New Multivariate Approach Including Automatic Selection of Calibration Samples and Quantification of Uncertainties*; Springer: Dordrecht, The Netherlands, 2015; pp. 507–534.
57. Lê, S.; Josse, J.; Husson, F. FactoMineR: An R Package for Multivariate Analysis. *J. Stat. Softw.* **2008**, *25*, 1–18. [[CrossRef](#)]
58. Wang, Z.; Li, R.; Yang, S.; Bai, F.; Mei, X.; Zhang, J.; Lu, K. Comparison of detrital mineral compositions between stream sediments of the Yangtze River (Changjiang) and the Yellow River (Huanghe) and their provenance implication. *China Geol.* **2019**, *2*, 169–178. [[CrossRef](#)]
59. Tian, S.; Li, Z.; Wang, Z.; Jiang, E.; Wang, W.; Sun, M. Mineral composition and particle size distribution of river sediment and loess in the middle and lower Yellow River. *Int. J. Sediment. Res.* **2021**, *36*, 392–400. [[CrossRef](#)]
60. Harden, T.M.; Ryberg, K.R.; Connor, J.E.O.; Friedman, J.M.; Kiang, J.E. Geological Paleostage Indicators. In *Historical and Paleoflood Analyses for Probabilistic Flood Hazard Assessments—Approaches and Review Guidelines*; Science Publishing Network, Tacoma Publishing Service Center: Oregon, OR, USA, 2021; pp. 9–26.
61. Hu, G.; Huang, C.C.; Zhou, Y.; Pang, J.; Zha, X.; Guo, Y.; Zhang, Y.; Zhao, X. Extreme paleoflood events 3200–3000 a BP in the Jingyuan–Jingtai reaches of the upper Yellow River, China. *Holocene* **2016**, *26*, 790–800. [[CrossRef](#)]
62. Wan, H.; Huang, C.; Pang, J. Major elements in the Holocene loess-paleosol sequence in the upper reaches of the Weihe River valley, China. *J. Arid Land* **2016**, *8*, 197–206. [[CrossRef](#)]
63. Chen, Y.; Huang, C.C.; Zhang, Y.; Zhou, Y.; Zha, X.; Wang, N.; Shang, R.; Rong, X.; Jia, Y.N.; Wang, H. Palaeoflood events during the last deglaciation in the Yellow River source area on the northeast Tibetan Plateau. *Geol. J.* **2021**, *56*, 4293–4309. [[CrossRef](#)]
64. Zwoliński, Z. Sedimentology and geomorphology of overbank flows on meandering river floodplains. *Geomorphology* **1992**, *4*, 367–379. [[CrossRef](#)]
65. Kidder, T.R.; Zhuang, Y. Anthropocene archaeology of the Yellow River, China, 5000–2000 BP. *Holocene* **2015**, *25*, 1602–1623. [[CrossRef](#)]
66. Zhang, Y.; Huang, C.C.; Pang, J.; Zha, X.; Zhou, Y.; Wang, X. Holocene palaeoflood events recorded by slackwater deposits along the middle Beiluohe River valley, middle Yellow River basin, China. *Boreas* **2015**, *44*, 127–138. [[CrossRef](#)]
67. Yao, Z.; Shi, X.; Qiao, S.; Liu, Q.; Kandasamy, S.; Liu, J.; Liu, Y.; Liu, J.; Fang, X.; Gao, J.; et al. Persistent effects of the Yellow River on the Chinese marginal seas began at least ~880 ka ago. *Sci. Rep.* **2017**, *7*, 2827. [[CrossRef](#)] [[PubMed](#)]
68. Lombardi, R.; Davis, M.A.L. Incorporating alluvial hydrogeomorphic complexities into paleoflood hydrology, magnitude estimation and flood frequency analysis, Tennessee River, Alabama. *J. Hydrol.* **2022**, *612*, 128085. [[CrossRef](#)]
69. Gelder, A.V.; Berg, J.H.V.D.; Cheng, G.; Xue, C. Overbank and channelfill deposits of the modern Yellow River delta. *Sediment. Geol.* **1994**, *90*, 293–305. [[CrossRef](#)]
70. Yu, S.; Li, W.; Zhou, L.; Yu, X.; Zhang, Q.; Shen, Z. Human disturbances dominated the unprecedentedly high frequency of Yellow River flood over the last millennium. *Sci. Adv.* **2023**, *9*, eadf8576. [[CrossRef](#)]
71. Yu, S.; Li, C.; Chen, X.; Jin, G.; Fang, H. Rates of Organic Carbon Burial in a Floodplain Lake of the Lower Yellow River Area during the Late Holocene. *Radiocarbon* **2014**, *56*, 1129–1138. [[CrossRef](#)] [[PubMed](#)]
72. Chen, S.; Qiang, L.; Zhang, F.; Li, X. Spatial and temporal distribution characteristics of earthen fort ruins in the lower reaches of the Yellow River and their relations with floods. *Sci. Geogr. Sin.* **2020**, *40*, 1202–1209. (In Chinese with English Abstract)
73. Lan, H.; Peng, J.; Zhu, Y.; Li, L.; Pan, B.; Huang, Q.; Li, J.; Zhang, Q. Research on geological and surficial processes and major disaster effects in the Yellow River Basin. *Sci. China Earth Sci.* **2022**, *65*, 234–256. [[CrossRef](#)]

Disclaimer/Publisher’s Note: The statements, opinions and data contained in all publications are solely those of the individual author(s) and contributor(s) and not of MDPI and/or the editor(s). MDPI and/or the editor(s) disclaim responsibility for any injury to people or property resulting from any ideas, methods, instructions or products referred to in the content.